Journal of Alloys and Compounds 849 (2020) 156628

Contents lists available at ScienceDirect

Journal of Alloys and Compounds

journal homepage: http://www.elsevier.com/locate/jalcom

A route towards enhanced UV photo-response characteristics of SnO_2/*p*-Si based heterostructures by hydrothermally grown nanorods

Kenan Ozel [a, b, *], Abdullah Atilgan [b], Nur Efşan Koksal [c], Abdullah Yildiz [b]

[a] Department of Electrical and Energy, GAMA Vocational School, Ankara University, Ankara, Turkey
[b] Department of Energy Systems Engineering, Faculty of Engineering and Natural Sciences, Ankara Yıldırım Beyazıt University, Ankara, Turkey
[c] Department of Electrical and Electronics Engineering, Faculty of Engineering and Natural Sciences, Ankara Yıldırım Beyazıt University, Ankara, Turkey

ARTICLE INFO

Article history:
Received 9 June 2020
Received in revised form
24 July 2020
Accepted 3 August 2020
Available online 14 August 2020

Keywords:
Heterojunction
UV photodiode
SnO_2
Nanorods

ABSTRACT

Integrating nanorods (*NRs*) into the structure of *p-n* heterojunction-based devices proposes a promising approach to overcome limited light absorption and charge transfer in optoelectronic devices. Herein, a new design scheme is demonstrated to improve the UV photo response properties of the heterojunction photodiodes. This design contains a spin-coated SnO_2 thin film underneath hydrothermally grown SnO_2 *NRs*. The *NRs* play versatile roles in enhancing the light trapping and providing direct pathway for electron transport, while thin film provides vertically aligned *NRs* formation and high-quality junction creation. The resulting structure offers an improvement in light harvesting and photo response characteristics of the devices. A photoresponsivity of 110 mA/W and a photosensitivity of 5.3 are observed in $SnO_{2\text{-NRs}}/SnO_2/p$-Si heterostructure. This structure can be a promising candidate for UV sensing applications owing to its high responsivity, sensitivity and easy fabrication process.

© 2020 Elsevier B.V. All rights reserved.

1. Introduction

UV light has some positive effects on the life of human beings by killing microorganisms; yet more exposure might cause some illnesses such as cancer or cataracts. To detect UV signal effectively, special detectors can be used [1]. The photodiodes, being a kind of photodetectors, based on *p-n* heterojunction have received considerable attention for the next generation optoelectronic industry. They have a great potential in a wide variety of areas, including security, diagnosis, screening, detecting, and UV communication; and they play a commercial role in the field of novel sensors and optoelectronic devices [2]. Wide band gap semiconductors such as ZnO, TiO_2, Ga_2O_3, and SnO_2 have been extensively studied for UV photodetection owing to their high transparency and visible blindness [3–5]. SnO_2, with a wide bandgap of 3.6 eV, is a promising candidate as a transparent coating *n*-type layer for photodiode and detector applications due to its low cost, high chemical and radiation stability and low resistance [6]. Therefore, it has been employed for various electronic devices such as solar cells, sensors, displays and transistors [7,8]. Xinhua et al. [9] stated that achieving high performance in photodetectors based on nanostructured SnO_2 is limited due to the surface defects and oxygen impurities adsorbed by the surface of SnO_2. Jing et al. [10] reported that the performance of UV photodetectors may be improved with fabrication in an inert environment, eliminating high concentration of surface impurities. In brief, researchers have devoted many efforts to enhance poor performance of photodetectors based on SnO_2. As a consequence, fabrication of different architectures of devices may be an effective way to reach high performance in photodetectors based on SnO_2. Hydrothermal method, spray pyrolysis, sputtering, pulse laser deposition, sol-gel spin coating, and chemical vapor deposition techniques have been used to integrate SnO_2 layers onto *p*-Si wafers. The sol-gel technique and hydrothermal method are superior over others since very homogenous thin films and nanostructures can be achieved with low cost and good reproducibility under moderate reaction conditions [11].

In the work reported herein, to have a *p-n* heterojunction, *n*-type SnO_2 was deposited onto the polished surface of the *p*-Si wafer by using the aforementioned two methods. The photodiodes constructed based on SnO_2 NRs with various layers of SnO_2 demonstrated promising results in terms of photoresponsivity reaching a value of 110 mA/W. It is noteworthy that such a remarkable value is higher than that of *p-n* photodiodes based on SnO_2 reported by

* Corresponding author. Department of Electrical and Energy, GAMA Vocational School, Ankara University, Ankara, Turkey.
E-mail address: kenan.ozel@ankara.edu.tr (K. Ozel).

https://doi.org/10.1016/j.jallcom.2020.156628
0925-8388/© 2020 Elsevier B.V. All rights reserved.

other groups [12], which indicates the significance of the proposed $SnO_{2\text{-}NRs}/SnO_2/p$-Si structured heterojunction photodiodes in the present study.

2. Experimental procedure

SnO_2/p-Si, $SnO_{2\text{-}NRs}/p$-Si and $SnO_{2\text{-}NRs}/SnO_2/p$-Si structured heterojunction photodiodes were investigated in this work (The details were given in Table 1). These devices are also denoted by *PD1*, *PD2* and *PD3*, respectively. A single side polished *p*-Si substrate (525 μm thickness and (100) surface orientation) was employed as an absorber layer. To eliminate surface contamination and native oxide layer, Piranha cleaning standard and HF dipping were applied to dice Si samples (1 × 1 cm^2). SnO_2 coating solution was synthesized using Tin (II) chloride dehydrate ($SnCl_2.2H_2O$) as a precursor, monoethanolamine (C_2H_7NO) as a stabilizer and 2-methoxyethanol ($C_3H_8O_2$) as a solvent [8]. After mixing these chemicals, the obtained solution was stirred for 2 h to get a clear and homogenous solution. The prepared SnO_2 solution was spin-coated (for 30 s at 2000 rpm) on cleaned Si to fabricate *PD1* and *PD3* structure. The deposition process was repeated two times and samples were annealed for 1 h at 450 °C to get a thin film. For the fabrication of SnO_2 nanorod layer of *PD2* and *PD3*, cleaned *p*-Si and SnO_2 deposited; *p*-Si (SnO_2/p-Si) samples were put in a stainless steel autoclave. Thereafter, synthesized SnO_2 solution was poured in this reactor and then heated at 95 °C for 6 h. Afterwards, the entire unpolished (back) surface of samples was etched with hydrofluoric acid to remove unwanted grown solution. Upon the etching process, Ag paste was screen-printed onto the etched surface of samples with a shadow mask. Ag printed samples were annealed in a tube oven at 150 °C for 10 min. After obtaining back ohmic contacts, the front surface of samples was finger-printed with Ag paste by using specially designed shadow mask, having 0.35 cm spaced grid-fingers of 0.08 cm width and 0.1 cm length. Fig. 1 represents the schematic illustration of $SnO_{2\text{-}NRs}/SnO_2/p$-Si heterojunction photodiode (*PD3*). Table 1 shows the summary of fabrication characteristics of these devices.

The crystal structure and optical properties of the SnO_2 films deposited on the glass substrates were measured using a Rigaku Miniflex 600 X-Ray diffractometer (XRD) and Shimadzu 1700 double beam UV−Vis spectrophotometer, respectively. The surface morphology and structure of SnO_2 nanorods were investigated via scanning electron microscope (SEM, Hitachi SU5000). The current−voltage (*I*−*V*) characteristics of the photodiodes were carried out in the dark and under UV-C (254 nm) illumination power of 1.85 mW/cm^2 with computerized Keithley 2400 source meter.

3. Results and discussion

To investigate the crystal structure of SnO_2 film, the prepared SnO_2 solution was coated on a glass. SnO_2 film has hexagonal wurtzite structure whose peak position is consistent with previous reports [13] (not given here). Fig. 2 shows the optical absorbance spectra of SnO_2 thin film and $SnO_{2\text{-}NRs}$ grown on SnO_2 thin films. The inset figure depicts $(\alpha h\nu)^2$ versus $(h\nu)$ (Tauc's) plot of SnO_2 thin film and $SnO_{2\text{-}NRs}$ grown on SnO_2 thin films for determination of band gap (E_g) value. The transmittance spectra of the emitter layer of devices (*PD1* and *PD3*) indicate that deposited film and structure show relatively high transparency of 72 and 75% in the visible region, respectively. The E_g values of SnO_2 thin film and $SnO_{2\text{-}NRs}$ grown on SnO_2 thin films are found to be 3.6 eV and 3.9 eV, respectively, using the Tauc's plot. The band gap (E_g) value of $SnO_{2\text{-}NRs}$ grown on SnO_2 thin film is larger than that of SnO_2 thin film with a considerable shift of 300 meV. Various theoretical models, such as quantum confinement effect [14], free-exciton collision [15], surface states [16], and Burstein−Moss (BM) effect [17], have been suggested to explain why the band gap value of nanostructures increases (blue shift of E_g). According to the many reports given in literature [17−21], this blue shift of E_g is caused by the BM effect. BM effect is an important phenomenon in n-type semiconductors and causes the shift in the E_g to higher energies [19]. In this effect, the increase of carrier concentration causes that the Fermi level moves into the conduction band, leading to enlargement in band gap [22]. Especially, a long duration of hydrothermal growth leads to nonstoichiometric distribution of Sn and O atoms due to the consumption of oxygen ion in the reactor. The defficiency of oxygen atoms in lattice induces the increase of carrier concentration, triggering the movement of Fermi level. Hence, the increase in band gap value of $SnO_{2\text{-}NRs}$ deposited in this work can be ascribed to the BM effect. Consequently, with the growth of SnO_2 nanostructures on the SnO_2 thin film, the increase in E_g value indicates the enhancement in optical properties of devices based on nanostructures.

Cross-sectional SEM images of SnO_2 nanostructures deposited on *p*-Si substrates with/without SnO_2 thin films, known as seeding layers, are depicted in Fig. 3. Cross-sectional SEM images reveal that SnO_2 nanostructures are in the form of nanorods (*NRs*). It should be mentioned that the presence of hydrothermally grown SnO_2 *NRs* plays a key role in the light trapping effect which is important for photosensitive devices, as we will discuss later. Moreover, it is noteworthy to say that the presence of a SnO_2 seeding layer coated on *p*-Si provides more uniform growth of vertically aligned *NRs*.

The energy-band alignment of n-SnO_2/p-Si heterojunction is constructed based on the Anderson model and depicted in Fig. 4 under UV an illumination condition at reverse applied bias. As observed in this diagram, the electron affinities for n-SnO_2 and *p*-Si are taken as 4.53 and 4.05 eV and the band gap values of n-SnO_2 and *p*-Si are assumed to 3.6 and 1.12 eV, respectively [23]. Thereby, the difference between electron affinity and energy band gap of these two materials leads to the creation of electron and hole barrier height. This barrier height maintains equilibrium between carriers in two regions. Considering the band gap (E_g) and electron affinity (χ) values of Si and SnO_2, the offset of conduction-band (ΔE_c) and valence-band (ΔE_v) were calculated as 0.48 eV and 2.96 eV using the equations of $\Delta E_c = \chi_{SnO_2} - \chi_{pSi}$ and $\Delta E_v = (E_{gSnO_2} - E_{gSnO_2}) + \Delta E_c$. As obviously seen, the conduction band offset (ΔE_c) is lower than the valance band offset (ΔE_v). Hence, the electron flow from n-SnO_2 to *p*-Si is much more than the hole flow in the reverse direction. After growing SnO_2 nanorods, the increase in bandgap value causes a high valance band offset, which reduces the saturation current under reverse applied bias in the dark.

As observed in Fig. 5, the working principle of $SnO_{2\text{-}NRs}/SnO_2/p$-Si heterojunction photodiode under UV illumination at reverse applied bias can be comprehended. Once the light within the range of <317 nm (E_{gSnO_2-NR}=3.9 eV) impinges on the device, it is absorbed by the $SnO_{2\text{-}NRs}$ layer, and the remaining spectrum (317 nm<λ < 1100 nm) can reach the n-SnO_2 seed layer and *p*-Si.

Table 1
Fabrication characteristics of fabricated devices.

Samples	*PD1*	*PD2*	*PD3*
Structure	SnO_2/p-Si	$SnO_{2\text{-}NRs}/p$-Si	$SnO_{2\text{-}NRs}/SnO_2/p$-Si
Method	SC-M	HTD-M	HDT-M/SC-M
Experimental Condition	30 s, 2000 rpm	6h, 95 °C	6h, 95 °C/30s, 2000 rpm
Thickness of film (nm)	80 nm	–	80 nm
Average size of *NRs* (μm)	–	6.08 x 0.78	6.93 x 0.76

*SC-M: Spin coating method, *HTD-M: Hydrothermal deposition method.

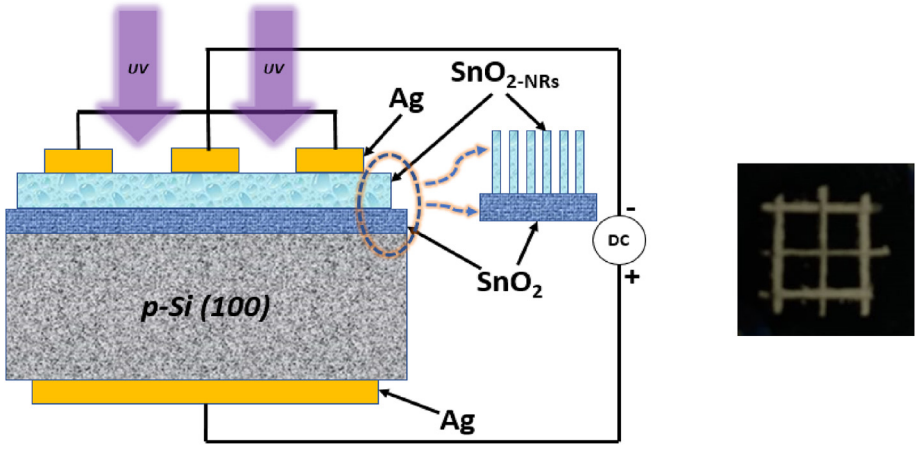


Fig. 1. a. Schematic representation of Ag/$SnO_{2\text{-}NRs}$/SnO_2/p-Si/Ag heterojunction photodiode b. Picture of one of the fabricated devices.

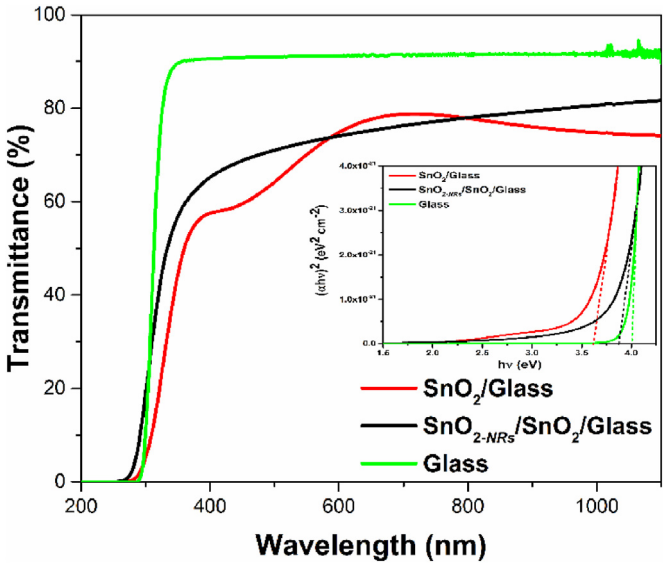


Fig. 2. The optical transmittance profile of SnO_2 thin film and $SnO_{2\text{-}NRs}$ grown on SnO_2 thin films. The inset figure displays the Tauc's plots to determine the band gap value of SnO_2 film $SnO_{2\text{-}NRs}$ grown on SnO_2 thin films.

The photons absorbed in the depletion layer lead to generation of electron-hole (*e-h*) pairs. Once they diffuse in opposite directions and reach the depletion layer, they drift under the effect of the built-in electric field occurring in the depletion layer. At the end of this process, a photocurrent is produced. The magnitude of this current depends on the width of the depletion layer, the magnitude of the built-in electric field, penetration depth of the incident photons, diffusion length and drift velocity of electron and holes, interface states and internal resistances. The value of width of the depletion layer typically varies between 0.19 and 0.33 μm for *n*-SnO_2/*p*-Si heterojunction devices [24]. Considering the thickness of the *n*-SnO_2 seed layer (~80 nm) and penetration depth ($1/\alpha$ = 110 nm, where α is the absorption coefficient at the wavelength corresponding to the bandgap edge of *n*-SnO_2) of incoming light in fabricated devices, one can evaluate that the penetration depth of incident light lets *e-h* pairs form within the depletion layer. This is desirable for photo-sensitive devices due to the lower recombination losses.

The semi-log plot *I–V* characteristics of *PD1*, *PD2* and *PD3* with and without UV-C irradiation is presented in Fig. 6. As observed from Fig. 6, all devices show rectifying behavior. At low forward bias voltages, current on a semi-log scale increases linearly with increasing forward bias voltages. However, when the applied forward bias is large enough, it deviates from linearity due to factors such as series resistance (R_s) and interface states [25]. After illumination of UV light, the increase in the photocurrent of fabricated heterojunction photodiodes is well distinguished especially at the reverse bias region because of the change in minority carriers. This increase in current under reverse bias is a good indicator for high-performance UV photodiodes which can be used for UV sensing applications. Among the fabricated photodiodes, it is noticeable that *PD3* has the most light-sensitive devices. This might be due to the enhancement of light trapping in the presence of $SnO_{2\text{-}NRs}$, causing in an improvement of the photon-harvesting efficiency and improvement in charge transport properties. With the presence of

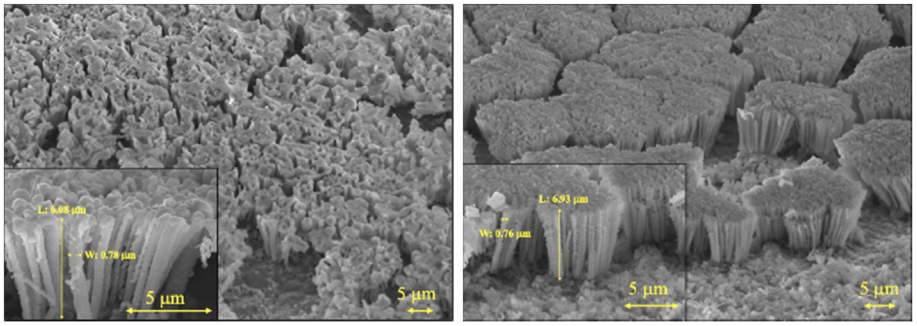


Fig. 3. SEM images of SnO_2 *NRs* deposited on **(a)** *p*-Si substrate **(b)** SnO_2 seed layer coated *p*-Si substrate.

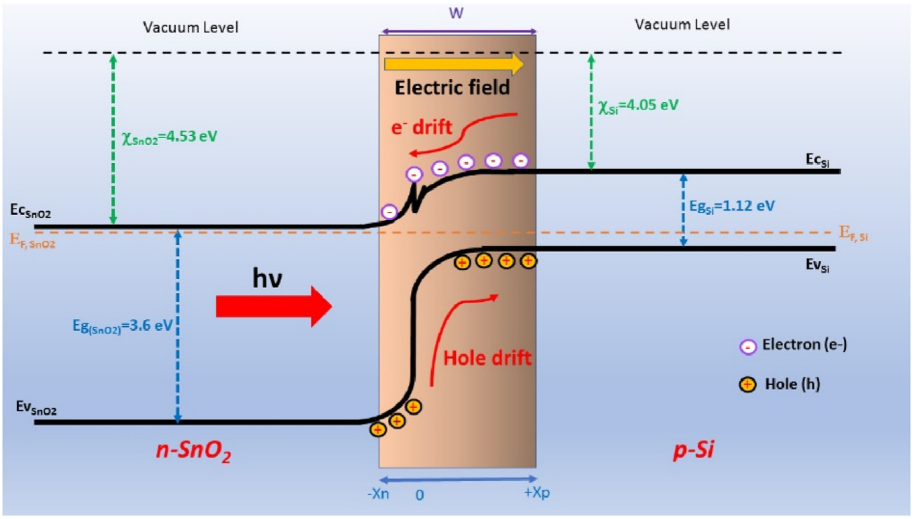


Fig. 4. The energy-band alignment of n-SnO_2/p-Si heterojunction under UV illumination condition at reverse applied bias.

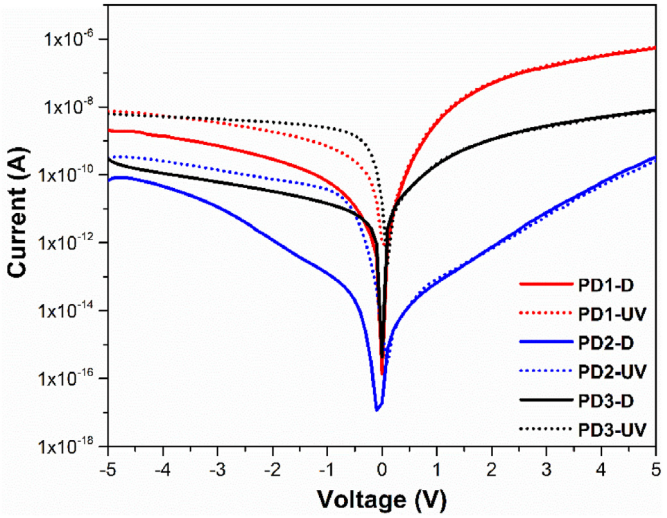


Fig. 5. The semi-log plot current-voltage characteristics of the photodiodes (*PD1* (red colored curves), *PD2* (blue colored curves), *PD3* (black colored curves)). (For interpretation of the references to color in this figure legend, the reader is referred to the Web version of this article.)

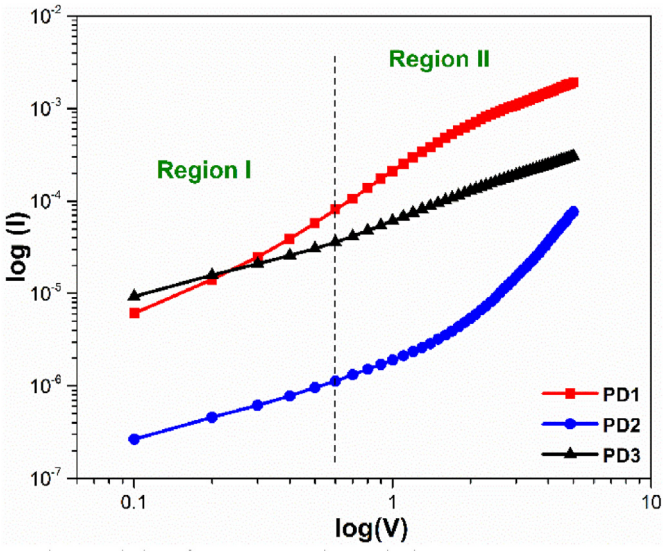


Fig. 6. Double logarithmic plot of *I*–*V* characteristics of PD1, PD2 and PD3 devices.

nanorods in the structure, the expansion of bandwidth and the guidance to the separated electrons enable the device to benefit from more incoming UV light; and at the same time, it provides a more effective photocurrent formation with low recombination rate. Moreover, the seed layer has an important effect on the charge transfer mechanism in the device. The presence of a seed layer might improve the transport parameters such as recombination rate, diffusion coefficient and length [26].

Diode parameters such as saturation current (I_s), ideality factor (n) and zero-bias barrier height ($Ø_{bi}$) were determined using the semi-logarithmic plotted current-voltage characteristics. The current-voltage characteristics can be expressed by Ref. [3],

$$I = I_s\left[\exp\left(\frac{qV}{nkT}\right) - 1\right] \tag{1}$$

Ideality factor can be determined by,

$$n = \frac{q}{kT}\frac{dV}{dln(I)} \tag{2}$$

Zero bias barrier height can be calculated by,

$$Ø_{bi} = \frac{kT}{q}\ln\left(\frac{AA^*T^2}{I_s}\right) \tag{3}$$

where I_s, q, n, k, T, A and A^*denote saturation current, charge of electron, ideality factor, Boltzmann's constant, temperature, effective diode area and effective Richardson's constant, respectively. The calculated values of I_s, n and $Ø_{bi}$ for the three fabricated devices are given in Table 2. *PD3* has partially reduced saturation current and relatively lower ideality factor values compared to other two devices, implying relatively high-quality junction formation. The values of barrier height of the devices are compatible with the literature [8]. The ideality factor values are found to be higher than unity, possibly due to the existence of various conduction

Table 2
Electrical parameters of the devices.

Samples	I_s (μA)	n	φ_{bi}* (eV)	φ_{bi}** (eV)	φ_{bi}*** (eV)	R_s* (kΩ)	R_s** (kΩ)	R_s*** (kΩ)
PD1	1.700	3.5	0.70±0.3	0.69±0.2	0.70±0.3	4 ±0.7	3.4±0.2	2.5 ±1
PD2	0.077	4.5	0.78±0.4	0.77±0.1	0.76±0.2	392±50	313±13.9	236±94
PD3	0.810	2.8	0.72±0.3	0.68±0.2	0.71 ±0.3	14.3±2.2	13.6±3.7	24.4±9.76

*From Eq. **(3, 4)** **From Eq. **(5, 6)** ***From Eq. **(7, 8, 9)**.

mechanisms, interface states, interface trap distribution, and inhomogeneous barrier height [27]. Therefore, one can expect a deviation from the general diode equation [25].

To figure out the transport mechanism of the devices, double logarithmically plotted forward *I–V* characteristics are shown in Fig. 6, generally separated into two distinct regions, represented as low (region I) and high voltages (region II). In region I, an ohmic behavior for all devices is observed with slopes slightly higher than unity (~1.3), indicating that the dominant conduction mechanism is tunneling [28]. If there is an exponential increase in current in the region II, this region shows the following relation: $I \sim exp(mV)$, where m refers to the slope of the *I–V* curve. It demonstrates that trap-filled limit voltage and space charge-limited current mechanisms are dominant transport mechanisms in region II [29]. In region II, the value of m exponentially increases (m~2.0) for *PD2*. Explicitly, *PD2* deviates from ohmic behavior when it enters into the high voltages. This deviation might be owing to the existence of an insulating layer at the junction region [30]. However, *PD1* and *PD3* persistently represent the ohmic behaviour for the two regions, as well.

At high forward bias, non-linear *I–V* characteristics are attributed to the series resistance (R_s), affecting the electrical characteristics and current loss of devices. For devices with high value of R_s, the *I–V* curve shows non-linear forward deviation and has a broad curvature. To achieve better performance for the devices, a minimum value of R_s is desired. R_s stems from front/back contacts, resistivity of layers, non-uniform inter-facial state and barrier height [31]. Different approaches, such as; the generalized diode equation's law, Cheung& Cheung's method and Norde method, are performed to find out R_s and $Ø_{bi}$ values of diodes. Three independent methods were used to evaluate electrical parameters of fabricated devices to make an accurate determination of the diode's parameters. It is reported that the results of these ways should be compatible with each other to indicate reliable values of parameters [32]. The value of $R_s$can be calculated to reflect voltage drop using Eq. (1),

$$\frac{dV}{d\ln(I)} = \frac{n\,k\,T}{q} + I\,R_s \tag{4}$$

The value of $R_s$can be also extracted from the equation given by Cheung & Cheung [33] using the function of *H(I)*,

$$H(I) = V - n\frac{kT}{q}\ln\left(\frac{I}{AA^*T^2}\right) \tag{5}$$

where the value of $Ø_{bi}$can be estimated from *H(I)*;

$$H(I) = nØ_{bi} + IR_s \tag{6}$$

The graphs of *dV/d(lnI)* and *H(I)* versus *I* are shown in Fig. 7 (a) and (b). The graphs of *dV/d(lnI)*, the slope of *x*-axis(I) and intercept of *y*-axis(I) are calculated as $R_s$and nkT/q. The slope of the *x*-axis(I) and intercept of the *y*-axis(I) of these graphs give the values of $R_s$and $n\,Ø_{bi}$for the devices by taking into account Cheung & Cheung's method. There is another method to determine these parameters proposed by Norde [34] and generalized by Bohlin [35] from the following equation (7),

$$F(V,\alpha) = \frac{V}{\alpha} - \frac{1}{\beta}\ln\left(\frac{I(V)}{AA^*T^2}\right) \tag{7}$$

where α and β refer to arbitrary constants (greater than n) and $\frac{q}{kT}$, respectively. To obtain the values of R_s and $Ø_{bi}$, the following equations can also be utilized:

$$Ø_{bi} = F_{min}(V,\alpha) + \frac{\alpha - n}{n}\left(\frac{V_{min}}{\alpha} - \frac{1}{\beta}\right) \tag{8}$$

$$R_s = \frac{(\alpha - n)}{\beta I_{min}} \tag{9}$$

where F_{min} is defined as the minimum point in the $F(V,\alpha)$ *vs* V graph and V_{min}, I_{min} are corresponding voltage and current values, respectively. The plot of $F(V,\alpha)$versus voltage is presented in Fig. 7 c.

All calculated parameters of the devices are given in Table 2. It is noteworthy that the values of parameters calculated with these three methods are in good agreement with each other. The differences in parameters stem from the application of these methods. The Norde method is performed for all parts of the forward bias region; while the generalized diode equation's and Cheung & Cheung's method are applied to a limited part of the forward bias region. Hence, the values of parameters calculated by the Norde method are affected by all factors such as interface state and resistivity. Also, the determination of the minimum point of the Norde's function is difficult task, as uncertainly estimated points can cause some inconsistency especially in series resistance values [33,36]. The minimum points of the Norde's function of our devices are easily determined and specified. As a consequence, the possible inconsistency has been eliminated. One can conclude that there is a correlation between device structure and electrical properties. According to Table 2, *PD1* has the smallest value of R_s among others. A high value of $Ø_{bi}$ results in a reduction in I_s. Although, the values of $R_s$found here are relatively low compared to the literature [11,37], we can rule out *PD2* with its undesired high value of R_s. Lower value of n and relatively lower value of R_s render *PD3* a suitable structure for light-sensitive applications.

PD3 deserves more discussion because of its superior performance over its counterparts. In its architecture, the presence of the seed layer positively affects the formation and distribution of nanostructures. Hydrothermally grown *NRs* provide higher light trapping and high surface to volume ratio [38]. For this reason, depositing of *NRs* on *p*-Si with a seed layer boosts the performance of devices.

The UV sensing properties of fabricated photodiodes, namely, the ratio of photo to dark current at a certain reverse voltage (photo-sensitivity ($PS = \frac{I_{ph}}{I_d}$)) and the ratio of photocurrent to power intensity of incoming light (photo-responsivity ($PR = \frac{I_{ph}}{P_{in}}$)) are determined as the figure of merits of the devices. Here, I_{ph}, I_d and P_{in}

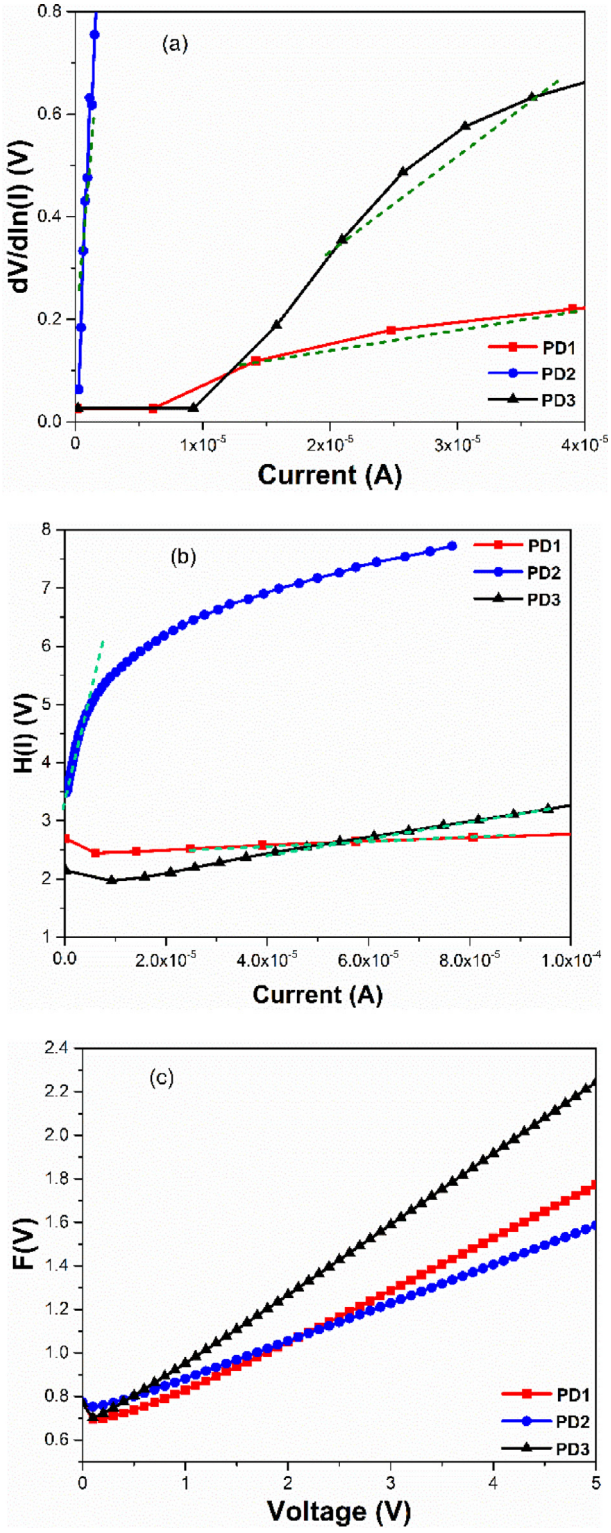


Fig. 7. (a) *dV/dln(I)* versus *I* (Eq. (4)) and **(b)** H(*I*) versus *I* (Eq. (5)) plots of the devices **c)** F(V) versus V (Eq. (7)) plot of the devices.

stand for photocurrent, dark current and incident power intensity, respectively. The value of *PS* is found as 1.8, 2.1 and 5.3 at -4V for *PD1*, *PD2* and *PD3*, respectively. The value of *PR* is obtained to be 62, 19 and 110 mA/W at -4V for *PD1*, *PD2* and *PD3*, respectively. The photoresponsivity data of some *p-n* heterojunction devices based on metal-oxide/Si has been reported in the literature (see Table 3).

Table 3
Comparison of the characteristic parameters for photodiodes reported in this study and previous works.

Structure	*PR* (mA/W)	References
SnO_2/*p*-Si	62±7	This work
$SnO_{2\text{-NR}}$/*p*-Si	19±1	This work
$SnO_{2\text{-NR}}/SnO_2$/*p*-Si	110±3	This work
n-ZnO_{NWs}/*p*-Si	70	[41]
SnO_2/CuZnS	28	[12]
TiO_2/*p*-Si_{NW}	230	[42]
n-TiO_2/*p*-Si	33	[43]
n-SnO2/Si_{NWs}	346	[44]
n-$TiO_{2\text{-NW}}$/*p*-Si	34	[45]
n-ZnO_{NRs}/*p*-*Si*	380	[46]
n-ZnO/*p*-Si	62	[47]

It is noteworthy to say that the responsivity value of devices directly depends on the photocurrent, since fabricated three devices are undergone to the same optical power. The photocurrent value of devices is affected by two factors, which are absorption of incoming light and efficient charge transport. The responsivity is affected by the parameters of photo-generated free carrier concentration and conduction cross section [39]. Whereas the former directly relates to the photon absorption, the latter is substantially influenced by the presence of defect states. Firstly, the formation of shallow junction between $SnO_{2\text{-NR}}$ and *p*-Si reduces the separation of carriers. Moreover, the increased defect states (especially vacancies and voids in nanostructures) creates discontinuities in the photo-generated charge transport and hence adversely affects the effective conduction cross section. Further, the presence of surface states might trap carriers and create recombination centers. Thus, the conduction and collection of carriers significantly reduce [40]. Therefore, the decrease in responsivity of $SnO_{2\text{-NR}}$/*p*-Si can be attributed to the lower amount of photo-generated carriers (owing to the inefficient charge transfer stemming from the non-uniformly growth of nanorods and the formation of shallow junction) and reduced conduction cross section (owing to the increased defect states). As a consequence, the deposition of SnO_2 seed layer mitigates all these negative effects by providing the formation of high-quality junction, allowing uniform growth of nanostructures and reducing the defect states of layers. It is obvious that *PD3* provides better performance than others. Therefore, the architecture of *PD3* should be considered as a good candidate for UV detection. Finally, more investigations are needed to further evaluate the performance of devices based on SnO_2.

4. Conclusion

In order to have heterojunction, various layers of SnO_2 were examined after combining with *p*-Si. The integration of the $SnO_{2\text{-NRs}}$ layer enhanced light harvesting and facilitated charge transport. Three methods were utilized to extract important parameters such as barrier height and series resistance of the devices. The parameters demonstrated consistency with each other. The best performance was obtained with the design of $SnO_{2\text{-NRs}}/SnO_2$/*p*-Si heterojunction in terms of photosensitivity (5.3 at −4 V) and photoresponsivity (110 mA/W at −4 V) to UV light illumination. Our findings undoubtedly reveal that $SnO_{2\text{-NRs}}/SnO_2$/*p*-Si heterostructure should be taken into account for metal-oxide based heterojunction devices especially in their UV sensing applications.

CRediT authorship contribution statement

Kenan Ozel: Conceptualization, Methodology, Data curation, Writing - original draft. **Abdullah Atilgan:** Visualization,

Investigation. **Nur Efşan Koksal:** Investigation, Resources. **Abdullah Yildiz:** Supervision, Writing - review & editing, and Editing.

Declaration of competing interest

The authors declare that they have no known competing financial interests or personal relationships that could have appeared to influence the work reported in this paper.

Acknowledgment

The work is based on the K.O's Ph.D. Thesis.

References

[1] Daoyou Guo, et al., Self-powered ultraviolet photodetector with superhigh photoresponsivity (3.05 A/W) based on the GaN/Sn: Ga_2O_3 pn junction, ACS Nano 12 (12) (2018) 12827–12835.
[2] Yanru Xie, et al., A self-powered UV photodetector based on TiO_2 nanorod arrays, Nanoscale research letters 8 (1) (2013) 188.
[3] Nur Efsan Koksal, Sbeta Mohamed, Abdullah Yildiz, GZO/Si photodiodes exhibiting high photocurrent-to-dark-current ratio, IEEE Trans. Electron. Dev. 66 (5) (2019) 2238–2242.
[4] Z.K. Yildiz, et al., Enhancement of efficiency of natural and organic dye sensitized solar cells using thin film TiO_2 photoanodes fabricated by spin-coating, J. Photochem. Photobiol. Chem. 368 (2019) 23–29.
[5] Takayoshi Oshima, et al., Vertical solar-blind deep-ultraviolet Schottky photodetectors based on β-Ga2O3 substrates, APEX 1 (1) (2008), 011202.
[6] Tülay Serin, et al., Electron–electron interactions in Sb-doped SnO_2 thin films, J. Electron. Mater. 39 (8) (2010) 1152–1158.
[7] M.A.M. Ahmed, et al., Effect of Sm doping ZnO nanorods on structural optical and electrical properties of Schottky diodes prepared by chemical bath deposition, Mater. Sci. Semicond. Process. 79 (2018) 53–60.
[8] Yuanxi Lu, et al., A boron and gallium co-doped ZnO intermediate layer for ZnO/Si heterojunction diodes, Appl. Surf. Sci. 428 (2018) 61–65.
[9] Xinhua Pan, et al., High responsivity ultraviolet detector based on novel SnO 2 nanoarrays, RSC Adv. 9 (64) (2019) 37201–37206.
[10] Jing Wu, et al., Colossal ultraviolet photoresponsivity of few-layer black phosphorus, ACS Nano 9 (8) (2015) 8070–8077.
[11] Yasemin Caglar, et al., Determination of the electronic parameters of nanostructure SnO2/p-Si diode, Microelectron. Eng. 86 (10) (2009) 2072–2077.
[12] Jian Cai, et al., Self-Powered n-SnO2/p-CuZnS core–shell microwire UV photodetector with optimized performance, Adv. Opt.Mater. 6 (15) (2018) 1800213.
[13] S.G. Ansari, et al., A novel method for preparing stoichiometric SnO 2 thin films at low temperature, Rev. Sci. Instrum. 80 (4) (2009), 045112.
[14] Yunbo Lv, et al., Controllable synthesis of ZnO nanoparticles with high intensity visible photoemission and investigation of its mechanism, Nanotechnology 24 (17) (2013) 175702.
[15] Yuri D. Glinka, et al., Size effect in self-trapped exciton photoluminescence from SiO 2-based nanoscale materials, Phys. Rev. B 64 (8) (2001), 085421.
[16] Chun-Wei Chen, et al., Anomalous blueshift in emission spectra of ZnO nanorods with sizes beyond quantum confinement regime, Appl. Phys. Lett. 88 (24) (2006) 241905.
[17] Y.H. Yang, et al., Physical mechanism of blue-shift of UV luminescence of a single pencil-like ZnO nanowire, Nano Lett. 7 (12) (2007) 3879–3883.
[18] A. Yildiz, E. Ozturk, A. Atilgan, et al., An understanding of the band gap shrinkage in Sn-doped ZnO for dye-sensitized solar cells, J. Electron. Mater. 46 (2017) 6739–6744.
[19] Tiangui You, et al., Fabrication and optical properties of needle-like ZnO array by a simple hydrothermal process, Mater. Lett. 66 (1) (2012) 246–249.
[20] G.H. Lee, et al., Blue shift in room temperature photoluminescence from photo-chemical vapor deposited ZnO films, Thin Solid Films 386 (1) (2001) 117–120.
[21] Ruijin Hong, et al., Influence of different post-treatments on the structure and optical properties of zinc oxide thin films, Appl. Surf. Sci. 242 (2005) 3–4, 346-352.
[22] Elias Burstein, Anomalous optical absorption limit in InSb, Phys. Rev. 93 (3) (1954) 632.
[23] Rui Chen, et al., A SnO_2 Nanoparticle/nanobelt and Si Heterojunction Light-Emitting Diode, 2010.
[24] S. Karadeniz, et al., The energy distribution of the interface state density of SnO2/p-Si (1 1 1) heterojunctions prepared at different substrate temperatures by spray deposition method, Appl. Surf. Sci. 246 (2005) 1–3, 30-35.
[25] İlke Taşçıoğlu, et al., Charge transport mechanisms and density of interface traps in MnZnO/p-Si diodes, J. Alloys Compd. 590 (2014) 157–161.
[26] Mahmoud Samadpour, Improving the parameters of electron transport in quantum dot sensitized solar cells through seed layer deposition, RSC Adv. 8 (46) (2018) 26056–26068.
[27] S. Monza Faraz, et al., Interface state density of free-standing GaN Schottky diodes, Semicond. Sci. Technol. 25 (9) (2010), 095008.
[28] S.M. Faraz, M. Willander, Q. Wahab, Interface state density distribution in Au/n-ZnO nanorods Schottky diodes, in: IOP Conference Series: Materials Science and Engineering, vol. 34, IOP Publishing, 2012. No. 1.
[29] Mustafa A. Ahmed, et al., Influence (Ce and Sm) co-doping ZnO nanorods on the structural, optical and electrical properties of the fabricated Schottky diode using chemical bath deposition, J. Alloys Compd. 810 (2019) 151929.
[30] N. Zebbar, et al., Structural, optical and electrical properties of n-ZnO/p-Si heterojunction prepared by ultrasonic spray, Mater. Sci. Semicond. Process. 14 (2011) 3–4, 229-234.
[31] H.G. Çetinkaya, et al., Electrical characteristics of Au/n-Si (MS) Schottky diodes (SDs) with and without different rates (graphene+ Ca 1.9 Pr 0.1 Co 4 O x-doped poly (vinyl alcohol)) interfacial layer, J. Mater. Sci. Mater. Electron. 28 (11) (2017) 7905–7911.
[32] Serhat Orkun Tan, Comparison of graphene and zinc dopant materials for organic polymer interfacial layer between metal semiconductor structure, IEEE Trans. Electron. Dev. 64 (12) (2017) 5121–5127.
[33] S.K. Cheung, N.W. Cheung, Extraction of Schottky diode parameters from forward current-voltage characteristics, Appl. Phys. Lett. 49 (2) (1986) 85–87.
[34] Herman Norde, A modified forward I-V plot for Schottky diodes with high series resistance, J. Appl. Phys. 50 (7) (1979) 5052–5053.
[35] K.E. Bohlin, Generalized Norde plot including determination of the ideality factor, J. Appl. Phys. 60 (3) (1986) 1223–1224.
[36] Enise Ayyildiz, et al., Effect of series resistance on the forward current-voltage characteristics of Schottky diodes in the presence of interfacial layer, Solid State Electron. 39 (1) (1996) 83–87.
[37] Muharrem Gökçen, et al., Forward and reverse bias current–voltage characteristics of Au/n-Si Schottky barrier diodes with and without SnO2 insulator layer, Phys. B Condens. Matter 406 (21) (2011) 4119–4123.
[38] Basavaraj S. Sannakashappanavar, et al., Seed layer effect on different properties and UV detection capability of hydrothermally grown ZnO nanorods over SiO2/p-Si substrate, Superlattice. Microst. 117 (2018) 503–514.
[39] J.A. Garrido, et al., Photoconductive gain modelling of GaN photodetectors, Semicond. Sci. Technol. 13 (6) (1998) 563.
[40] Monu Mishra, et al., Surface-engineered nanostructure-based efficient nonpolar GaN ultraviolet photodetectors, ACS Omega 3 (2) (2018) 2304–2311.
[41] Lei Luo, et al., Fabrication and characterization of ZnO nanowires based UV photodiodes, Sensor Actuator Phys. 127 (2) (2006) 201–206.
[42] Gopal Rawat, et al., Electrical and ultraviolet-A detection properties of E-beam evaporated n-TiO2 capped p-Si nanowires heterojunction photodiodes, IEEE Trans. Nanotechnol. 16 (1) (2016) 49–57.
[43] Sabah N. Mazhir, et al., UV photovoltaic detector based on Bi doped TiO2 fabricated by pulse laser deposition, Int. J. Adv. Res. 3 (5) (2015) 1060–1070.
[44] Saravanan Yuvaraja, et al., Ultraviolet detection properties of electrodeposited n-SnO 2 modified p-Si nanowires hetero-junction photodiode, J. Mater. Sci. Mater. Electron. 30 (8) (2019) 7618–7628.
[45] Saeideh Ramezani Sani, Analysis of optoelectronic properties of TiO2 nanowiers/Si heterojunction arrays, Chin. Phys. B 23 (10) (2014) 107302.
[46] N.H. Al-Hardan, et al., A wide-band UV photodiode based on n-ZnO/p-Si heterojunctions, Sensor Actuator Phys. 207 (2014) 61–66.
[47] J.Y. Lee, et al., Optimizing n-ZnO/p-Si heterojunctions for photodiode applications, Thin Solid Films 403 (2002) 553–557.